Far-Field Subwavelength Acoustic Computational Imaging with a Single Detector

Yuan Tian,[1] Hao Ge,[1] Xiu-Juan Zhang,[1] Xiang-Yuan Xu,[1,2] Ming-Hui Lu,[1,3,*] Yun Jing,[4] and Yan-Feng Chen[1,3]

[1] *National Laboratory of Solid State Microstructures and Department of Materials Science and Engineering, Nanjing University, Nanjing 210093, China*

[2] *The Institute of Acoustics of the Chinese Academy of Sciences, Beijing 100190, China*

[3] *Collaborative Innovation Center of Advanced Microstructures, Nanjing 210093, China*

[4] *Graduate Program in Acoustics, The Pennsylvania State University, University Park, Pennsylvania 16802, USA*

(Received 7 May 2022; revised 29 May 2022; accepted 31 May 2022; published 19 July 2022)

Acoustic imaging techniques suffer from the diffraction limit due to the loss of evanescent waves that carry subwavelength information of objects. To overcome the diffraction limit, the evanescent components have to be collected and measured. Most of the existing methods targeting this task rely on expensive detector arrays and inefficient near-field point-by-point scanning. Here, we propose and experimentally demonstrate the realization of a far-field acoustic subwavelength imaging method based on a single stationary detector. Specifically, we utilize a series of masks to structure the detected field, so that the evanescent wave information is encoded into the propagating waves due to spatial frequency convolution between the object and masks. Our study shows that, by combining the principles of computational imaging and metalens, high-quality images of a subwavelength object can be reconstructed in the far field, even in the presence of unwanted scatterers. Our work provides a robust method for far-field acoustic subwavelength imaging, which could bring possibilities for acoustic microscopy and could further be applied to medical ultrasonography, underwater sonar, and ultrasonic nondestructive evaluation.

DOI: 10.1103/PhysRevApplied.18.014046

I. INTRODUCTION

Acoustic imaging techniques have been widely used in areas including medical ultrasonic imaging [1,2], industrial nondestructive testing [3], and underwater sonar systems [4]. Traditional acoustic imaging methods generally rely on detector arrays or detector scanning to accurately measure the reflected, transmitted, or scattered acoustic field. These methods, however, have some drawbacks: while detector arrays are typically expensive and entail complex driving and receiving systems, detector scanning is inefficient and rely on scanning equipment. To address these challenges, it is highly desirable to develop a technique for acoustic imaging with a nonmoving single detector. The recent development in computational imaging may offer an elegant solution for imaging using a single-pixel detector [5–16]. By sequentially projecting a series of spatial patterns to filter or structure the detected fields and measuring the total transmitted or reflected wave intensity with a single-pixel detector, it is possible to reconstruct the spatial information of the object to be imaged.

On the other hand, acoustic imaging is inherently limited by the diffraction limit [17]. This is because the high spatial frequency information (i.e., subwavelength features) of an object is carried by evanescent waves, which decay exponentially as they propagate away from the object and therefore they cannot be detected in the far field. To obtain subwavelength resolution (below $\lambda/2$, where λ is the wavelength), one needs to recover the evanescent-wave components. In the past few decades, various approaches have been developed to realize subwavelength imaging beyond the diffraction limit. For instance, the near-field scanning technique [18,19] is able to collect the evanescent waves by working directly in the nearest proximity of the object. Recently, acoustic metamaterial-based lenses, such as negative-parameter metamaterials [20–23] and extremely anisotropic metamaterials [24–27], have been proposed to realize subwavelength imaging [20–31]. The dispersion relation and effective material properties of these metamaterials were engineered in a way to either amplify the evanescent waves or support the propagation of evanescent waves. By placing the acoustic metamaterial lenses in the near-field objects, the evanescent waves can be carried to the far field. However, once the evanescent waves exit the metamaterials, they will decay exponentially again. In addition, these methods also heavily rely

*luminghui@nju.edu.cn

on point-to-point detection or detector scanning, and they could be very susceptible to environmental interference. For example, irrelevant or unwanted scattering objects in the wave propagation path could adversely affect the signal-to-noise ratio of the imaging results.

In this work, by combining the principles of computational imaging and metalens, we propose and experimentally demonstrate an acoustic far-field subwavelength imaging system with a single detector. The masks placed on one side of the metalens are able to encode the evanescent waves of the object into the propagating waves and project them to the far field. High-quality images of subwavelength object with a resolution of $\lambda/57$ is demonstrated. In addition, we show that our method is able to recover the object information even in the presence of interfering scattering and the detector can be at a flexible distance that is many wavelengths away from the object.

II. RESULTS AND DISCUSSION

A. Principle of far-field subwavelength acoustic imaging

The principle of far-field subwavelength acoustic imaging is illustrated in Fig. 1. The imaging target here is a two-dimensional (2D) object of subwavelength size. When an incident acoustic wave impinges upon this object, the evanescent field is confined in the near field and decays exponentially with distance. As a result, the signals captured by a detector array in the far field will not contain any subwavelength information of the object [Fig. 1(a)]. Holey-structured acoustic metamaterials [24] have been used as a near-field imaging device by supporting the propagation of the evanescent waves inside its structures [Fig. 1(b)]. If the incident wave is at the Fabry-Perot resonance frequencies, subwavelength features of the object carried by the evanescent waves can be funneled through the metamaterials and reach the output surface. However, as soon as the evanescent waves leave the surface of the metalens, they will rapidly decay again and cannot propagate to the far field (see simulated imaging results in this case in Appendix A). In both examples in Figs. 1(a) and 1(b), the subwavelength object cannot be clearly imaged in the far field.

Instead, in our system shown in Fig. 1(c), a series of masks are sequentially placed at the output port of the metalens. The mask here is a 2D acoustic screen with subwavelength patterns. Due to spatial frequency convolution between the object and masks, the evanescent-wave components of the object can be encoded into propagating waves and this information is subsequently transmitted into the far field, which can be recovered by algorithms based on computational imaging. We explain the process of spatial frequency convolution as follows.

B. Theoretical analysis of evanescent waves in computational imaging

In our imaging system, the acoustic pressure field of the image plane in real space can be expressed as

$$\begin{aligned} p(x,y,z_i) = \{\{[p(x,y,z_o)U_o(x,y,z_o)] \\ \otimes_{x,y} h'(x,y,z_m-z_o)\}U_m(x,y,z_m)\} \\ \otimes_{x,y} h(x,y,z_i-z_m), \end{aligned} \tag{1}$$

where U_o and U_m are the transmission coefficients of the 2D object and mask, respectively; z_o, z_m, and z_i are the positions of the object, mask, and image plane, respectively; h and h' represent the acoustic point spread functions in the free space and the metalens, respectively.

For simplification, we assume the incident wave is the plane wave, so that $p(x,y,z_o)=1$. In addition, we assume that the metalens is a perfect imaging device, that is, the field from the input port of the metalens can be perfectly transmitted to the output port of the metalens. Then it follows that

$$p(x,y,z_i) = [U_o(x,y)U_m(x,y)]\otimes_{x,y}h(x,y,z_i-z_m). \tag{2}$$

According to Eq. (2), the acoustic pressure field of the image plane in the wave-vector domain can be expressed as

$$P(k_x,k_y,z_i) = [A_o(k_x,k_y)\otimes_{x,y}A_m(k_x,k_y)]H(k_x,k_y,z_i-z_m), \tag{3}$$

where A_o and A_m are the spectra of the object and the mask, respectively; H is the acoustic transfer function in the free space, which serves as a low-pass filter and is expressed as

$$H(k_x,k_y,z) = \begin{cases} e^{jz\sqrt{k^2-k_x^2-k_y^2}}, & \sqrt{k_x^2+k_y^2} \le k \\ e^{-\alpha z}\ (\alpha>0), & \sqrt{k_x^2+k_y^2} > k \end{cases}, \tag{4}$$

where $\alpha=\sqrt{k_x^2+k_y^2-k^2}$. If the propagating distance $z \gg \lambda$, $e^{-\alpha z}\to 0$.

Here, the spectrum of the object A_o can be divided into two parts: the propagating-wave components A_o^1 and the evanescent wave components A_o^2, as follows:

$$A_o(k_x,k_y) = A_o^1(k_x,k_y) + A_o^2(k_x,k_y). \tag{5}$$

Equation (3) can be then expressed as

$$\begin{aligned} P(k_x,k_y,z_i) = \{[A_o^1(k_x,k_y)+A_o^2(k_x,k_y)] \\ \otimes_{x,y}A_m(k_x,k_y)\}H(k_x,k_y,z_i-z_m). \end{aligned} \tag{6}$$

Equations (4) and (6) show that the evanescent-wave components of the object will affect the low-spatial-frequency

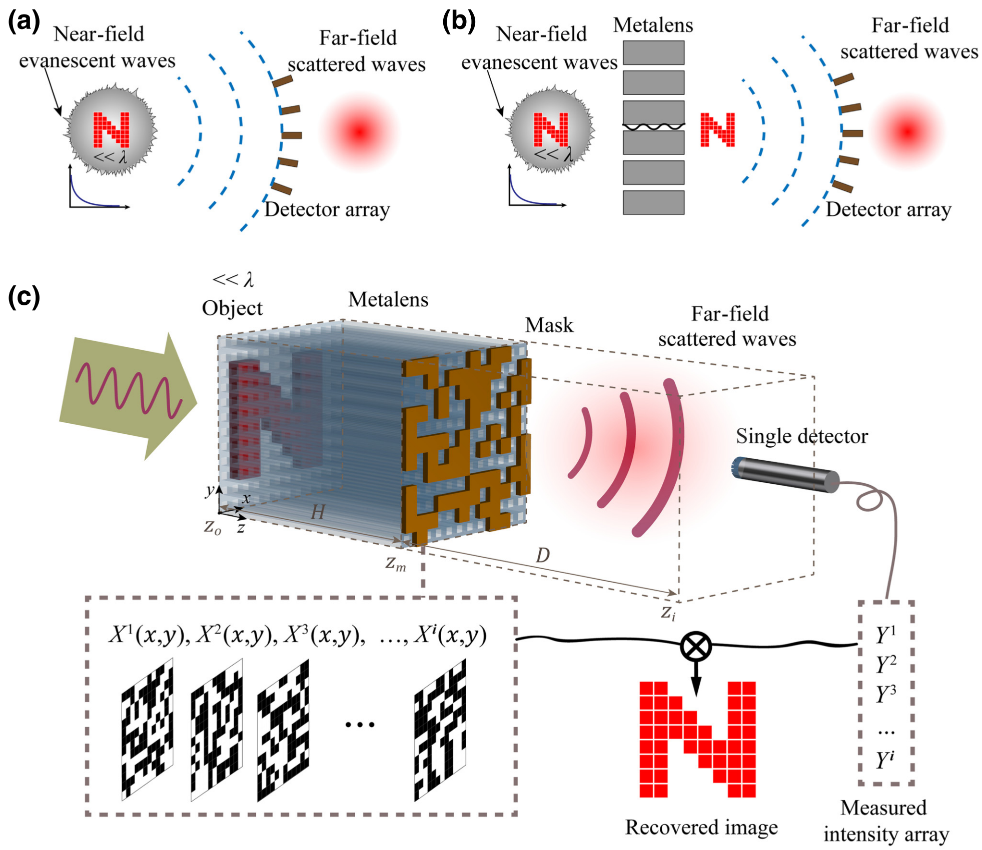

FIG. 1. Illustration of the proposed imaging system. (a) When an incident wave impinges over a subwavelength object, the evanescent field with high parallel momentum that contains subwavelength features of the object exhibits exponential decays with distance, therefore resulting in the loss of subwavelength information in the far field. (b) Holey structured metalens in the near field of the object allows the coupling of evanescent waves to propagating waves. But, evanescent fields will exponentially decay again as they leave the structure and cannot reach farther fields. (c) The proposed far-field imaging system is composed of a metalens, a series of masks, and a single-pixel detector. The metalens acts as a near perfect imaging device by reproducing the deep-subwavelength information of the detected object. The masks are used to encode the detected image intensities for different patterns. The single microphone is used to measure the intensity of the transmitted field, which is used to reconstruct the image of the object by combining the mask patterns.

components of the image plane. Therefore, due to the spatial-frequency convolution of the object and the mask, the evanescent waves of the object can be encoded into propagating waves of imaging plane and reach the far field. It is worth noting that while Eqs. (2)–(6) are still valid if the mask and the object exchange position, or if the mask is directly placed in the near field of the object, the metalens allows us to place the mask in a more flexible way.

Computational ghost imaging is able to reconstruct the image of the object by correlating a series of spatially resolved patterns and the corresponding total transmission intensity. The object information can be retrieved with the second-order intensity correlation defined [10] as

$$C(x,y) = \langle X^i_{\text{ref}}(x,y)Y^i\rangle_N - \langle X^i_{\text{ref}}(x,y)\rangle_N\langle Y^i\rangle_N. \tag{7}$$

Here, $X^i_{\text{ref}}(x,y)$ is the spatially resolved patterns in the ith measurement, which is known as *a priori*; Y^i is the total transmission intensity from the bucket measurement, denoted as the bucket intensity. $\langle\ldots\rangle_N$ denotes the ensemble average over a series of N measurements.

In traditional ghost imaging theory, the bucket intensity is contributed by all the components of the transmitted field containing the evanescent waves and the propagating waves. In our case, it can be expressed as

$$Y_{b1} = \iint |A_o(k_x,k_y)\otimes_{x,y}A_m(k_x,k_y)|^2 dk_x dk_y. \tag{8}$$

In the far field, however, the evanescent wave vanishes, and the bucket intensity is contributed by only the propagating waves, which can be expressed as

$$Y_{b2} = \iint_{\sqrt{k_x^2+k_y^2}\le k} |A_o(k_x,k_y)\otimes_{x,y}A_m(k_x,k_y)|^2 dk_x dk_y. \tag{9}$$

We compare the bucket intensity Y^i_{b1} and Y^i_{b2} for different mask patterns, as shown in Fig. 2. It can be seen that Y^i_{b1}

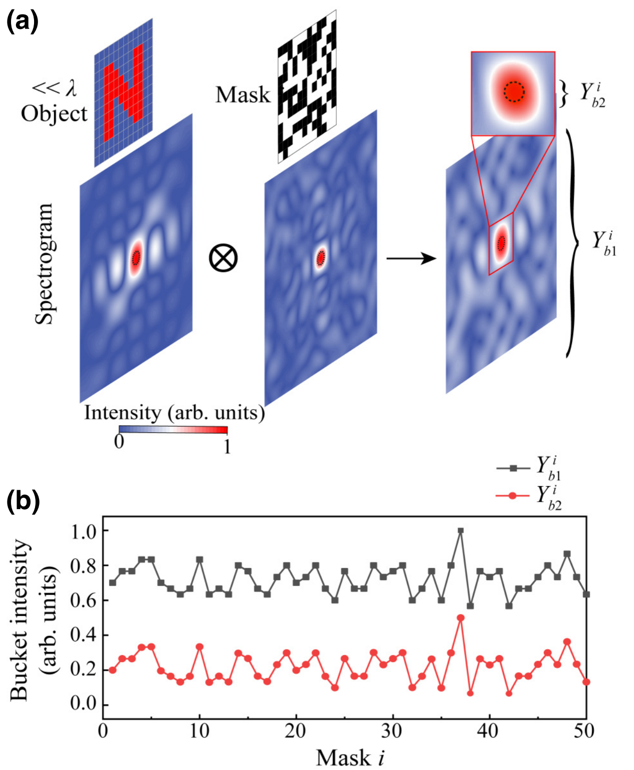

FIG. 2. Illustration of spatial frequency convolution between object and mask. (a) The subwavelength object "*N*" and mask here have a size of 0.21 **λ** × 0.21 **λ** and drawn on 12 × 12 pixels. The black dotted line in the spectrogram is the cutoff spatial frequency. After the convolution operation, we calculate the bucket intensity Y_{b1} and Y_{b2}. Y_{b1} is contributed by all the wave components and Y_{b2} is contributed by only the propagating wave components. (b) The bucket intensity with different mask.

and Y^i_{b2} follow the same variation trend, resulting in the same recovered image from Eq. (7). Therefore, the subwavelength features of the object can be realized only by detecting the intensity of the propagating waves even in the far field. Considering the deep subwavelength characteristics of the system, the emitted acoustic field can be regarded as a point-source radiation. As such, we can use a single-point measurement by a microphone instead of the bucket measurement.

C. Experimental imaging results

In our experiments, we consider three subwavelength objects shaped like the letters "*N*", "*J*," and "*U*" as the target images. Each letter has a size of 42×42 mm^2 and drawn on 12×12 pixels. Figure 3(a) shows the holey structured metalens. The dependence of the transmission coefficient versus parallel momentum and frequency is shown in Fig. 3(b), for the metalens with parameters $A = 3.5$ mm, $a = 1.75$ mm, and $H = 100$ mm. Flat dispersion in both the evanescent and propagating regions of the wave-vector space can be seen at the Fabry-Perot resonant frequencies ($m = 1$–4, corresponding to 1.72, 3.34, 5.15, 6.86 kHz). The modulus of the transmission coefficient on these lines is 1, indicating that full transmission will occur at the Fabry-Perot resonant frequencies. We choose the operating frequency as 1.72 kHz (corresponding to a wavelength of $\lambda = 200$ mm) for demonstration.

The masks have the same size and number of pixels with objects. The samples of the objects, metalens, and masks are fabricated by three-dimensional (3D) printing with commercial photopolymer materials, which can be regarded as perfectly rigid for airborne sound. To efficiently couple the evanescent waves, the objects and masks are placed in contact with the metalens directly. A speaker confined in a rigid square tube is used for exciting plane waves (see the details on the experimental setup in Appendix B).

For the choice of the mask patterns, random patterns are commonly used in computational imaging, but the number of its measurements for the reconstruction of an image with high quality is typically 10 times more than the amount of Nyquist limit (i.e., the number of image

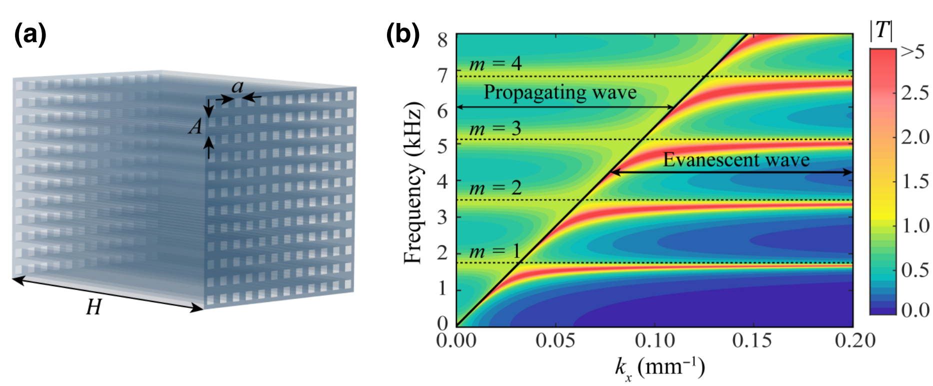

FIG. 3. Structure and properties of the metalens. (a) Schematic of the metalens. Geometrical parameters in our case are $A = 3.5$ mm, $a = 1.75$ mm, $H = 100$ mm. (b) The dispersion relations of the holey metalens in air. At the Fabry-Perot resonances frequencies ($m = 1$, 2, 3, 4), the modulus of transmission coefficient $|T|$ is 1.

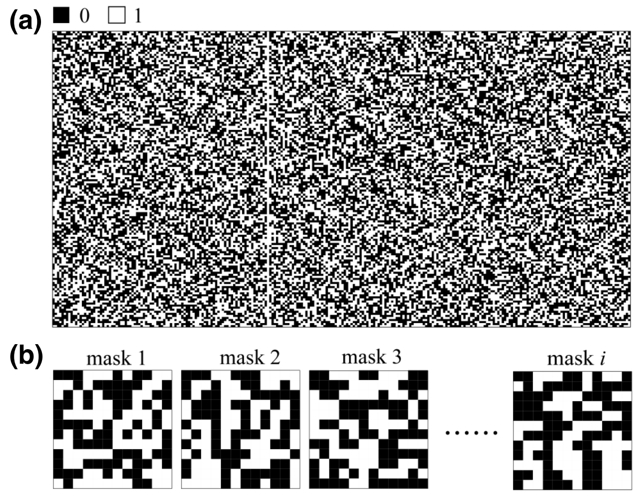

FIG. 4. The spatial information of masks. (a) 144×256 partial Hadamard matrix. (b) Spatial pattern of different masks.

pixels). In addition, various orthogonal patterns, such as Hadamard and Fourier patterns, have been proposed and demonstrated for their advantages in computational imaging with a low sampling ratio due to their orthogonality. Since 0–1 binary patterns contain only two elements "0" and "1," they can be conveniently used to design acoustic masks, where "1" indicates that the acoustic wave is allowed to transmit through the corresponding pixel of the masks and "0" means that the wave is blocked. Therefore, we consider the 0–1 binary patterns from a Hadamard matrix as the mask pattern. Note that the Hadamard matrix is a square matrix whose entries are either "1" or "−1" and its order can only be a power of 2. As such, we choose a partial Hadamard matrix and transform "−1" to "0". In our case, since the number of image pixel is 144, we choose the mask pattern from the 144×256 partial Hadamard matrix [Fig. 4(a)] and each column of the matrix (144 numbers) is rearranged into a 12×12 mask pattern [Fig. 4(b)].

Using Eq. (7), we obtain the reconstructed images from a series of measurements ($N = 256$). The distance between image plane and the output port of the metalens is denoted as D. Figures 5(b) and 5(c) show the imaging results of detecting in the near field ($D = 0.25\lambda$) and far field ($D = 2\lambda$), respectively. The resolution of these images is $\lambda/57$. It can be seen that the subwavelength characteristics of the recovered images are in good agreement with the target images, confirming the ability of our method to image the subwavelength object in the far field (more simulated imaging results at different distances are shown in Appendix A). It is worth mentioning that although we use 256 masks in our experiments, the number of masks required for imaging is not fixed and can be adjusted to the problem in hand.

We also investigate the performance of our method under environmental interference. In the experiment, we place two interfering objects in front of the detector, a steel

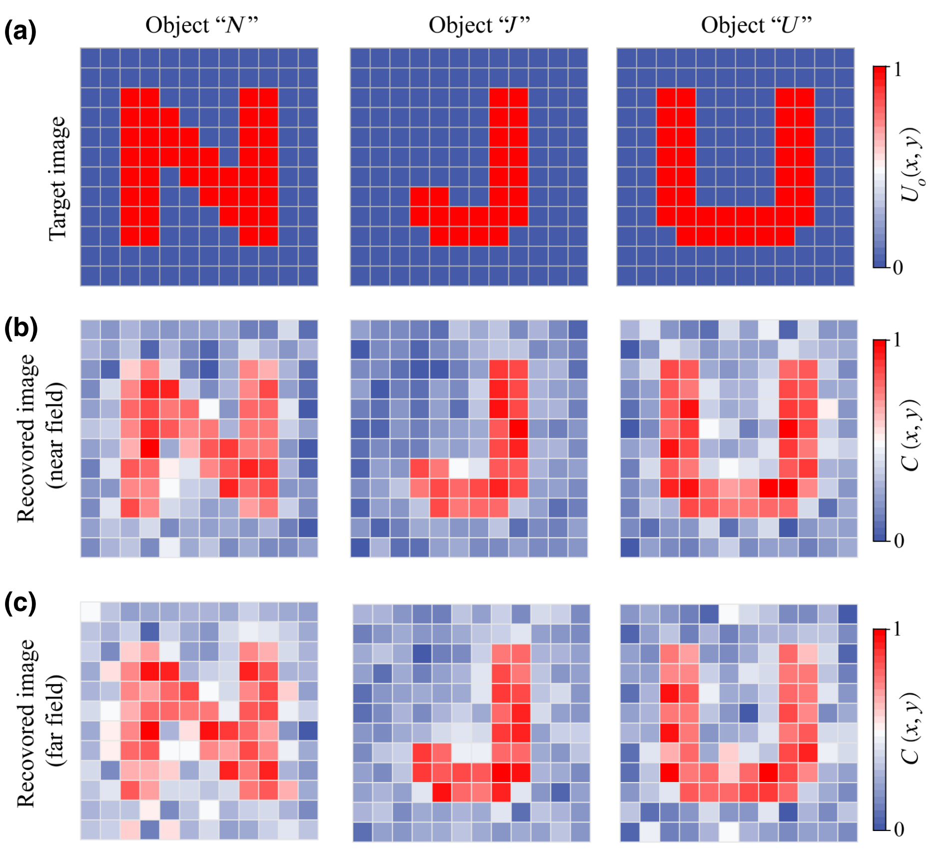

FIG. 5. Experimental results. (a) The target images. (b) Imaging results for detection in near field ($D = 0.25\lambda$). (c) Imaging results for detection in far field ($D = 2\boldsymbol{\lambda}$).

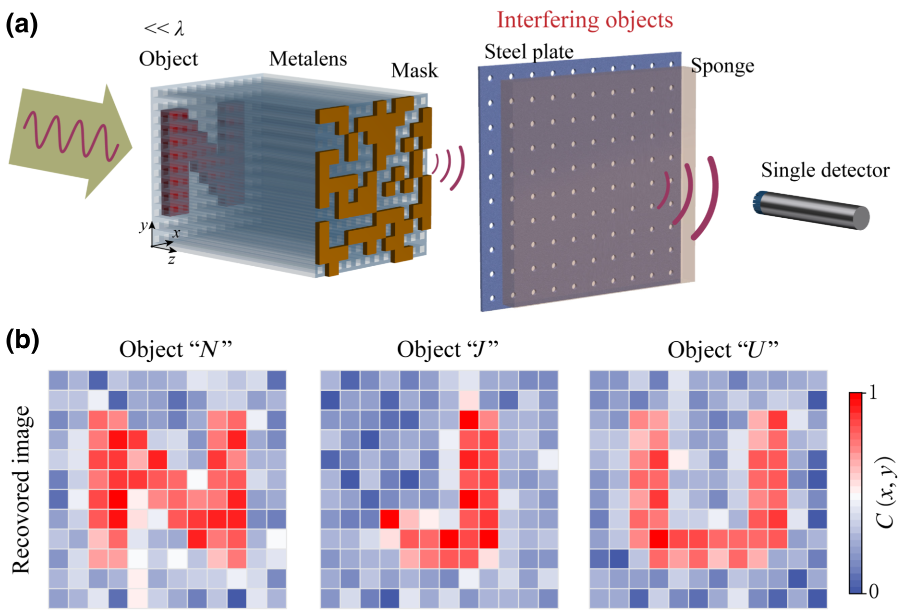

FIG. 6. Experimental imaging results under environmental interference. (a) Schematic diagram of the experimental system. (b) Imaging results under environmental interference ($D = 2\lambda$). D is the distance between image plane and the output port of the metalens.

plate with holes and a sponge [Fig. 6(a)]. The steel plate will strongly scatter the transmitted field, and the sponge will cause multiple scattering as well as sound absorption. For traditional point-to-point acoustic imaging, these unwanted environmental interferences could significantly reduce the signal to noise of the image. Figure 6(b) shows the experimental imaging results with interfering objects. We can clearly see the adverse effect of the scattering and absorption is significantly suppressed and bears virtually no influence on the quality of the images. This is because our method is based on the detection of the intensity of the propagating waves of the transmitted field, and the scattering and absorption effects in the far field will not affect the variation trend of the intensity of the propagating waves for different masks. Therefore, our method is robust against environmental interferences.

III. CONCLUSION

In conclusion, our experiments have successfully demonstrated far-field acoustic subwavelength imaging using a single detector. In addition to showing high-quality computational images of a subwavelength object with a resolution of $\lambda/57$, our results also suggest that this method is robust against unwanted scattering. Our method, therefore, can prove useful for acoustic microscopy and feature detection in a complex environment, such as through highly scattering media and tortuous propagation paths. Besides, the single detector can be at a flexible position, which is beneficial to practical applications. The system can be scaled to sizes of interest in ultrasonic medical imaging and nondestructive testing applications to increase the imaging resolution, offering great promise for applications in ultrasound imaging at subwavelength resolution.

The computational imaging method requires multiple measurements, resulting in long data-acquisition times. There are several ways to further reduce the data-acquisition time to enable fast imaging. For example, optimization algorithms such as compressed sensing [9] and machine learning [32,33] can significantly reduce the number of measurements required for imaging. Besides, frequency-division multiplexing-based metamaterials [34] enables one-shot computational imaging. Furthermore, 3D acoustic computational imaging may be realized through shape from shading with several single-pixel detectors [12] and time-of-flight technique [35,36].

ACKNOWLEDGMENTS

The work is supported by the National Key R&D Program of China (Grants No. 2017YFA0303702, No. 2018YFA0306200), the National Natural Science Foundation of China (Grants No. 51902151, No. 11625418, and No. 51732006). We also acknowledge the support from the Academic Program Development of Jiangsu Higher Education (PAPD).

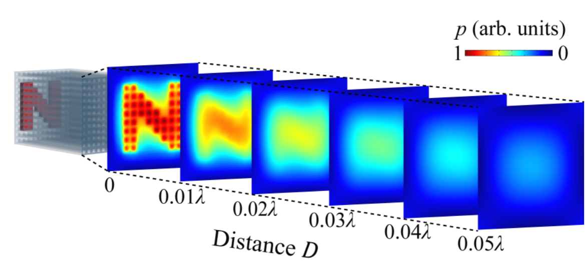

FIG. 7. Simulation of direct imaging at different detecting distances.

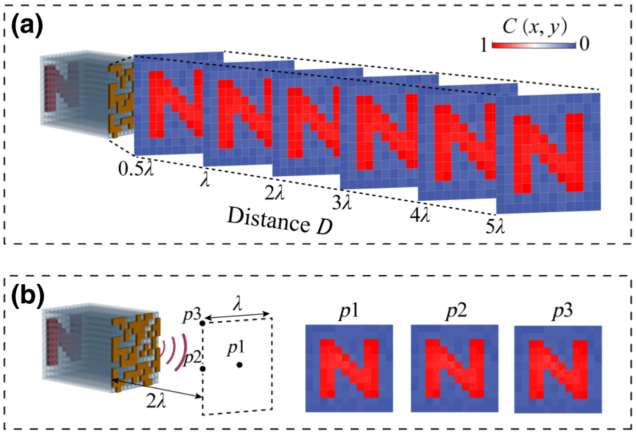

FIG. 8. (a) Simulation of computational imaging at different detecting distances. (b) Simulation of computational imaging at different detecting positions.

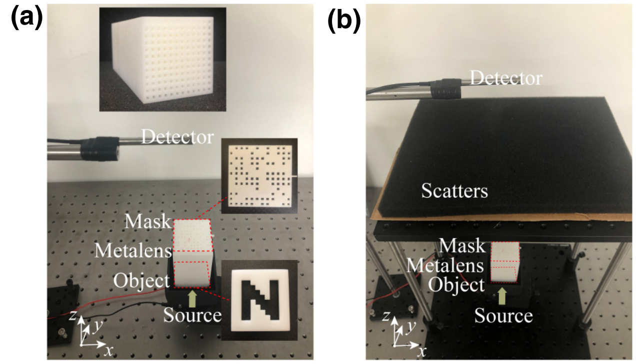

FIG. 9. Photos of the experimental setup. (a) Experimental setup without interfering objects. (b) Experimental setup under the interfering objects.

APPENDIX A: NUMERICAL SIMULATIONS OF DIRECT IMAGING AND COMPUTATIONAL IMAGING

To further verify our method, numerical simulations are adopted using the pressure acoustic module of a commercial finite-element simulation software (COMSOL Multiphysics). The mess density and sound velocity in air are chosen as 1.21 $\mathrm{kg/m^3}$ and 343 m/s, respectively. The photopolymer materials are treated as acoustically rigid boundaries.

For the direct imaging in Fig. 1(b), the simulated imaging results are shown in Fig. 7. The target object "N" has a size of $0.21\lambda \times 0.21\lambda$. The results show that the subwavelength features of the object can reach the output port of the metalens, but they disappear in the far field, because the evanescent waves exponentially decay as they leave the metalens. For the computational imaging, the simulated imaging results are shown in Fig. 8. We can clearly see that the computational imaging does not have a strict requirement on the position of the detector that can be in a flexible position.

APPENDIX B: DETAILS ON IMAGING OBJECTS AND EXPERIMENTAL SETUP

In the experiment, we use a 20-mm diameter speaker confined in a rigid square tube for the plane-wave incidence. An acoustic pressure probe (Brüel & Kjær 4939 0.25-in. microphone) is fixed on the image plane to detect the transmitted field. The collected signals are acquired a multifunction I/O device (National Instruments PCI-6251). The samples of objects, metalens, and masks are fabricated by 3D printing with commercial photopolymer materials

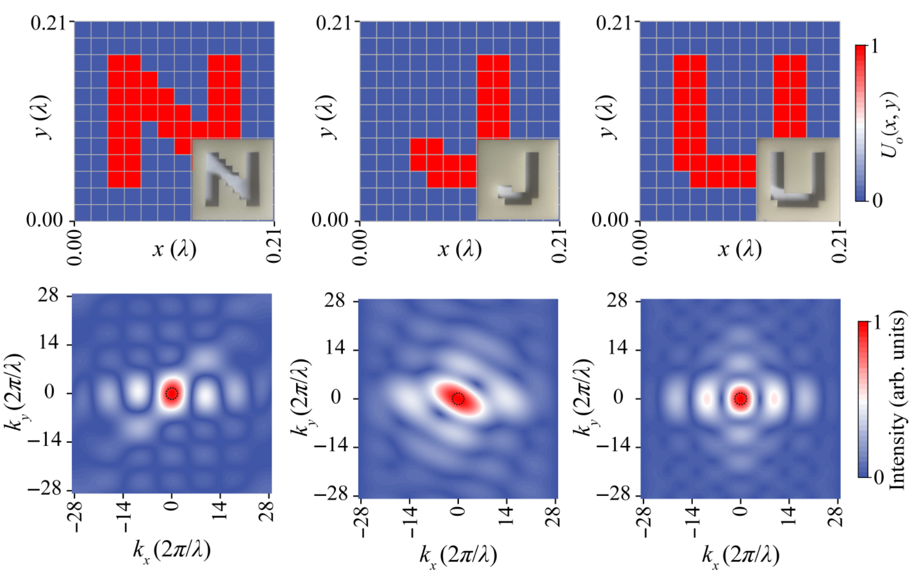

FIG. 10. Spectra of the images of "N", "J," and "U".

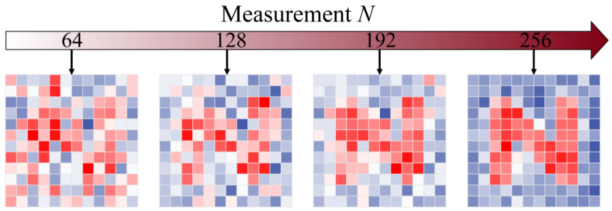

FIG. 11. Imaging results for a different number of measurements.

(modulus 2765 MPa, density 1.3 g/cm^3). The tolerance of the fabrication is 0.1 mm, which is less than 3% compared the pixel size in our case. The experiment setup is shown in Fig. 9.

The target images "N", "J," and "U" and its corresponding spectrogram are shown in Fig. 10, where the black dotted line in the spectrogram is the cutoff spatial frequency. It can be seen that for the subwavelength objects, there are a large number of evanescent-wave components, which play a dominant role in the imaging process. Figure 11 shows the imaging results for object "N" for a different number of measurements.

APPENDIX C: MASK ERROR AND IMAGING QUALITY

The imperfection of the masks in construction and location may cause measurement errors and impact imaging results. Here we discuss this impact as follows. For quantitative evaluation, we examine simulated data in this section.

First, we introduce the peak signal-to-noise ratio ($P_{\rm SNR}$) to quantitatively describe the quality of imaging results, as

$$P_{\rm SNR} = 10\,\log_{10}\left(\frac{M_{\max}^2}{M_{\rm MSE}}\right),$$

where $M_{\max}$ is the maximum pixel value of the image; normalized is applied in computing $P_{\rm SNR}$, giving $M_{\max}$ of 1. $M_{\rm MSE}$ is the mean square error, which reads

$$M_{\rm MSE} = \frac{1}{m \times n}\sum_{i,j}[C(x_i, y_i) - T(x_i, y_i)]^2,$$

where $C(x_i, y_i)$ and $T(x_i, y_i)$ are the pixel values of the reconstructed image and the target image, and $m \times n$ is the number of the pixels of the image.

Next, we discuss the influence of manufacturing tolerance and location error of masks on imaging quality. In the first case of Fig. 12(a), considering the manufacturing tolerance of the mask is δ ($\delta < $ a), the value of pixel "1" of the mask becomes a random value $p(1 - (\delta/a)^2 < p < 1)$. Figure 12(b) compares the imaging results for different manufacturing tolerance. The $P_{\rm SNR}$ values for $\delta/a = 0.1, 0.3, 0.5, 0.7,$ and 0.9 are calculated as 26.47, 18.82, 14.31, 11.60, and 9.97 dB, respectively. Furthermore, $P_{\rm SNR}$ of imaging results for different values of δ/a from 0.01 to 1 are shown in Fig. 12(c). Each value is calculated 100 times to obtain the error bar and the measurement number N is 256.We can clearly see that as manufacturing tolerance increases, the quality of imaging results decreases. In the second case of Fig. 12(a), considering the location error

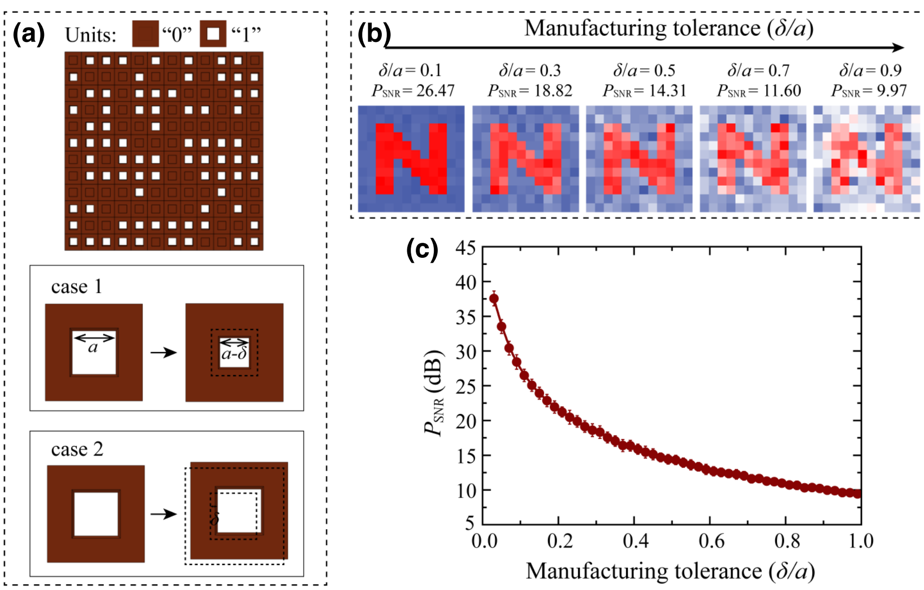

FIG. 12. (a) The model of masks. (b) Simulated imaging results for different manufacturing tolerances of masks. (c) $P_{\rm SNRs}$ with δ/a ranging from 0.01 to 1.

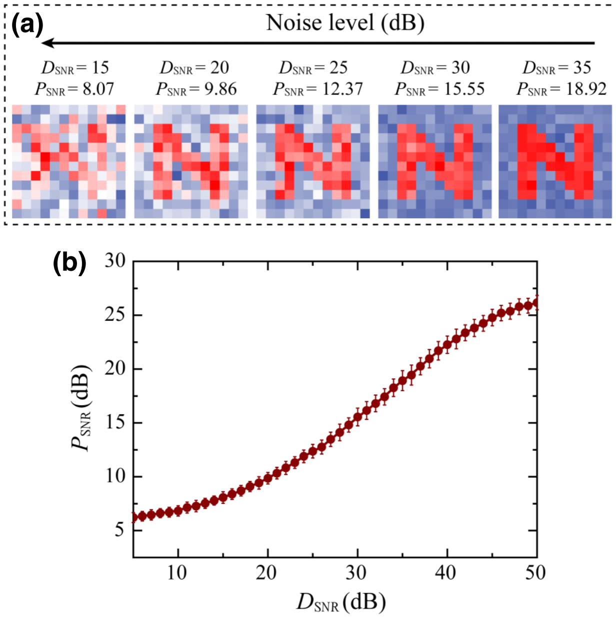

FIG. 13. Numerical results considering the noise term I^i_{noise}. (a) Computational imaging results for different noise levels. (b) P_{SNR} as a function of D_{SNR}.

of masks ($\delta < a$), all pixels “1” of the mask become a constant $q (0 < q < 1)$ due to the overall misalignment of the mask. In this case, the imaging results are not affected.

In our experiment, the masks are fabricated by 3D printing and the tolerance of fabrication is 0.1 mm, which is less than 3% compared to the pixel size. Therefore, the influence of manufacturing tolerance of the masks on the quality of imaging results can be ignored.

APPENDIX D: MEASUREMENT ERROR AND IMAGING QUALITY

There are measurement errors in the detection process such as background noise that can impact imaging results. To analyze the effect of noise, a time-varying noise term I^i_{noise} can be introduced in the detection process as $\hat{Y}^i = Y^i + I^i_{\text{noise}}$, where I^i_{noise} is random for each measurement. Below, we discuss the relationship between noise level and imaging results.

The detection signal-to-noise radio (D_{SNR}) are introduced to quantitatively describe the noise level, as

$$D_{\text{SNR}} = 10 \log_{10} \left(\frac{Y^i}{I^i_{\text{noise}}} \right).$$

The imaging results and the P_{SNR} for different D_{SNR} are shown in Fig. 13. We can clearly see that as the noise level increases, the image quality decreases.

[1] A. Fenster and D. B. Downey, 3-D ultrasound imaging: A review, IEEE Eng. Med. Biol. Mag. **15**, 41 (1996).
[2] A. Webb and G. C. Kagadis, Introduction to biomedical imaging, Med. Phys. **30**, 2267 (2003).
[3] J. Blitz and G. Simpson, *Ultrasonic Methods of Non-Destructive Testing* (Springer Science & Business Media, London, 1995).
[4] J. L. Sutton, Underwater acoustic imaging, Proc. IEEE **67**, 554 (1979).
[5] M. P. Edgar, G. M. Gibson, and M. J. Padgett, Principles and prospects for single-pixel imaging, Nat. Photonics **13**, 13 (2019).
[6] T. B. Pittman, Y. H. Shih, D. V. Strekalov, and A. V. Sergienko, Optical imaging by means of two-photon quantum entanglement, Phys. Rev. A **52**, R3429 (1995).
[7] D. V. Strekalov, A. V. Sergienko, D. N. Klyshko, and Y. H. Shih, Observation of Two-Photon “Ghost” Interference and Diffraction, Phys. Rev. Lett. **74**, 3600 (1995).
[8] J. H. Shapiro, Computational ghost imaging, Phys. Rev. A **78**, 061802 (2008).
[9] M. F. Duarte, M. A. Davenport, D. Takhar, J. N. Laska, T. Sun, K. F. Kelly, and R. G. Baraniuk, Single-pixel imaging via compressive sampling, IEEE Signal Process. Mag. **25**, 83 (2008).
[10] Y. Bromberg, O. Katz, and Y. Silberberg, Ghost imaging with a single detector, Phys. Rev. A **79**, 053840 (2009).
[11] B. Sun, S. S. Welsh, M. P. Edgar, J. H. Shapiro, and M. J. Padgett, Normalized ghost imaging, Opt. Express **20**, 16892 (2012).
[12] B. Sun, M. P. Edgar, R. Bowman, L. E. Vittert, S. Welsh, A. Bowman, and M. J. Padgett, 3D computational imaging with single-pixel detectors, Science **340**, 844 (2013).
[13] H. C. Liu, B. Yang, Q. Guo, J. Shi, C. Guan, G. Zheng, H. Mühlenbernd, G. Li, T. Zentgraf, and S. Zhang, Single-pixel computational ghost imaging with helicity-dependent metasurface hologram, Sci. Adv. **3**, e1701477 (2017).
[14] R. I. Stantchev, B. Sun, S. M. Hornett, P. A. Hobson, G. M. Gibson, M. J. Padgett, and E. Hendry, Non-invasive, near-field terahertz imaging of hidden objects using a single-pixel detector, Sci. Adv. **2**, e1600190 (2016).
[15] Y. Guo, B. Li, and X. Yin, Single-Shot Compressed Photoacoustic Tomographic Imaging with a Single Detector in a Scattering Medium, Phys. Rev. Appl. **13**, 044009 (2020).
[16] P. Kruizinga, Pim van der Meulen, A. Fedjajevs, F. Mastik, G. Springeling, Nico de Jong, J. G. Bosch, and G. Leus, Compressive 3D ultrasound imaging using a single sensor, Sci. Adv. **3**, e1791423 (2017).
[17] A. A. Maznev and O. B. Wright, Upholding the diffraction limit in the focusing of light and sound, Wave Motion **68**, 182 (2017).
[18] Earl G. Williams and J. D. Maynard, Holographic Imaging without the Wavelength Resolution Limit, Phys. Rev. Lett. **45**, 554 (1980).
[19] Y. Lee and E. G. Williams, Nearfield acoustic holography: I. Theory of generalized holography and the development of NAH, J. Acoust. Soc. Am. **78**, 1395 (1985).
[20] X. Zhang and Z. Liu, Superlenses to overcome the diffraction limit, Nat. Mater. **7**, 435 (2008).

[21] J. B. Pendry, Negative Refraction Makes a Perfect Lens, Phys. Rev. Lett. **85**, 3966 (2000).

[22] F. Lemoult, M. Fink, and G. Lerosey, Negative refractive index and acoustic superlens from multiple scattering in single negative metamaterials, Nature **525**, 77 (2015).

[23] V. M. García-Chocano, J. Christensen, and J. Sánchez-Dehesa, Negative Refraction and Energy Funneling by Hyperbolic Materials: An Experimental Demonstration in Acoustics, Phys. Rev. Lett. **112**, 144301 (2014).

[24] J. Zhu, J. Christensen, J. Jung, L. Martin-Moreno, X. Yin, L. Fok, X. Zhang, and F. J. Garcia-Vidal, A holey-structured metamaterial for acoustic deep-subwavelength imaging, Nat. Phys. **7**, 52 (2011).

[25] J. Christensen and F. J. García De Abajo, Anisotropic Metamaterials for Full Control of Acoustic Waves, Phys. Rev. Lett. **108**, 124301 (2012).

[26] J. Li, L. Fok, X. Yin, G. Bartal, and X. Zhang, Experimental demonstration of an acoustic magnifying hyperlens, Nat. Mater. **8**, 931 (2009).

[27] C. Shen, Y. Xie, N. Sui, W. Wang, S. A. Cummer, and Y. Jing, Broadband Acoustic Hyperbolic Metamaterial, Phys. Rev. Lett. **115**, 254301 (2015).

[28] B. Orazbayev and R. Fleury, Far-Field Subwavelength Acoustic Imaging by Deep Learning, Phys. Rev. X **10**, 031029 (2020).

[29] H. Ge, M. Yang, C. Ma, M. Lu, Y. Chen, and N. Fang, Breaking the barriers: Advances in acoustic functional materials, Natl. Sci. Rev. **5**, 159 (2018).

[30] S. A. Cummer, J. Christensen, and A. Alù, Controlling sound with acoustic metamaterials, Nat. Rev. Mater. **1**, 16001 (2016).

[31] G. Ma and P. Sheng, Acoustic metamaterials: From local resonances to broad horizons, Sci. Adv. **2**, e1501595 (2016).

[32] M. Lyu, W. Wang, H. Wang, H. Wang, G. Li, N. Chen, and G. Situ, Deep-learning-based ghost imaging, Sci. Rep. **7**, 1 (2017).

[33] Y. He, G. Wang, G. Dong, S. Zhu, H. Chen, A. Zhang, and Z. Xu, Ghost imaging based on deep learning, Sci. Rep. **8**, 1 (2018).

[34] J. Hunt, T. Driscoll, A. Mrozack, G. Lipworth, M. Reynolds, D. Brady, and D. R. Smith, Metamaterial apertures for computational imaging, Science **339**, 310 (2012).

[35] W. Gong, C. Zhao, H. Yu, M. Chen, W. Xu, and S. Han, Three-dimensional ghost imaging lidar via sparsity constraint, Sci. Rep. **6**, 26133 (2016).

[36] M. J. Sun, M. P. Edgar, G. M. Gibson, B. Sun, N. Radwell, R. Lamb, and M. J. Padgett, Single-pixel three-dimensional imaging with time-based depth resolution, Nat. Commun. **7**, 12010 (2016).